Circuit-field coupled finite element analysis method for an electromagnetic acoustic transducer under pulsed voltage excitation*

Hao Kuan-Sheng(郝宽胜), Huang Song-Ling(黄松岭)†,
Zhao Wei(赵 伟), and Wang Shen(王 珅)

State Key Laboratory of Power Systems, Department of Electrical Engineering, Tsinghua University, Beijing 100084, *China*

(Received 5 September 2010; revised manuscript received 9 January 2011)

This paper presents an analytical method for electromagnetic acoustic transducers (EMATs) under voltage excitation and considers the non-uniform distribution of the biased magnetic field. A complete model of EMATs including the non-uniform biased magnetic field, a pulsed eddy current field and the acoustic field is built up. The pulsed voltage excitation is transformed to the frequency domain by fast Fourier transformation (FFT). In terms of the time harmonic field equations of the EMAT system, the impedances of the coils under different frequencies are calculated according to the circuit-field coupling method and Poynting's theorem. Then the currents under different frequencies are calculated according to Ohm's law and the pulsed current excitation is obtained by inverse fast Fourier transformation (IFFT). Lastly, the sequentially coupled finite element method (FEM) is used to calculate the Lorentz force in the EMATs under the current excitation. An actual EMAT with a two-layer two-bundle printed circuit board (PCB) coil, a rectangular permanent magnet and an aluminium specimen is analysed. The coil impedances and the pulsed current are calculated and compared with the experimental results. Their agreement verified the validity of the proposed method. Furthermore, the influences of lift-off distances and the non-uniform static magnetic field on the Lorentz force under pulsed voltage excitation are studied.

Keywords: electromagnetic acoustic transducer, nondestructive testing, circuit-field coupling, finite element method

PACS: 81.70.Cv, 81.70.Ex, 41.20.–q **DOI:** 10.1088/1674-1056/20/6/068104

1. Introduction

Electromagnetic acoustic transducers (EMATs) have been an important ultrasonic non-destructive evaluation technique for electrically conducting materials.[1,2] EMATs have several distinct advantages over traditional piezoelectric transducers for many inspection applications requiring novel solutions. These advantages include: operation without a coupling fluid, non-contact operation, high temperature operation and ease of multi-mode ultrasonic generation.

EMATs consist of three sections: magnets, coils and specimens. In practical applications of EMATs, the coils of the transmitters and receivers are usually made by printed circuit board (PCB) or flexible print circuit (FPC) techniques for accurate dimensions, design, compact configuration and convenient application.[3] The coils of the transmitters are supplied by a high power amplifier. Permanent magnets are generally used instead of electromagnets to provide a strong biased magnetic field because permanent magnets are smaller and in no need of an extra power source.

Simulation analysis of practically applied EMATs is necessary for their analysis and optimal design.[3,4] Since the 1960s, a number of researchers have carried out simulation studies of EMATs. Thomson used an analytical method to calculate and analyse the performance of EMATs.[5,6] However, its accuracy was low because the analytical model was complicated and had many assumptions. With the increasing development of computer science, numerical calculation methods were applied for EMAT simulations. Ludwig and his students[7,8] modeled the transduction process of EMATs in terms of the interrelations in each physics field, on the assumption that the bias magnetic field was uniform, and neglecting the skin effect and proximity effect between the conductors in the coil. Then, the finite element method (FEM) was used to simulate the EMAT. Shapoorabadi *et al.*[9,10] found that the skin effect and proximity effect were remarkable between the conductors in the coil of the EMAT because the distance between the conductors was small and the

*Project supported by the National Natural Science Foundation of China (Grant No. 10974115).
†Corresponding author. E-mail: huangsling@tsinghua.edu.cn
© 2011 Chinese Physical Society and IOP Publishing Ltd

frequency of the exciting current was high. Neglecting the skin and proximity effects would result in inaccurate simulation results. Therefore, the eddy current in the conductors was added to Ludwig's model in order to improve the accuracy of the model. At the same time, there are other researchers who tried to use other methods to simulate EMATs,[11,12] but the results were unsatisfactory.

In the above simulated models and methods, the excitation signal of the coils is current. Simulated methods for EMATs under voltage excitation have not been investigated, which may be more useful for practical EMATs. Furthermore, the biased magnetic filed was assumed to be uniform, which is not the case for permanent magnets. Lastly, complex coil configurations made by PCB or FPC have not been simulated in present literatures.

In this paper, a complete EMAT model, comprising of coils, a permanent magnet and a non-ferromagnetic specimen was set up. Therefore, the non-uniform distribution of the biased magnetic field was considered. The performance of the EMATs were then simulated by the FEM method under the voltage excitation condition through circuit-field coupling. An actual EMAT with a two-layer two-bundle PCB coil, a rectangular permanent magnet and an aluminium specimen was simulated and analysed. Experimental results verify the validity of the proposed model and method.

2. Multi-field coupled equations of EMATs

2.1. Static magnetic field equations of the permanent magnet

There is no free current in the magnetic field of the permanent magnet. The magnetic field intensity $\boldsymbol{H}_0$ can be expressed by the negative gradient of scalar magnetic potential V_m

$$\boldsymbol{H}_0 = -\nabla V_\mathrm{m}. \tag{1}$$

The Maxwell equation and constitutive relation are

$$\boldsymbol{\nabla} \cdot \boldsymbol{B}_0 = 0, \tag{2}$$

$$\boldsymbol{B}_0 = \mu \boldsymbol{H}_0 + \boldsymbol{B}_\mathrm{r}, \tag{3}$$

where $\boldsymbol{B}_0$ is magnetic flux density, μ is permeability of medium, $\boldsymbol{B}_\mathrm{r}$ is residual flux density of the permanent magnet.

Substituting Eqs. (1) and (3) into Eq. (2), we obtain the Laplace equation of scalar magnetic potential

$$\boldsymbol{\nabla}^2 V_\mathrm{m} = \boldsymbol{\nabla} \cdot \boldsymbol{B}_\mathrm{r}. \tag{4}$$

If the permanent magnet is magnetized uniformly in certain direction, $\boldsymbol{B}_\mathrm{r}$ will be a constant vector. Thus

$$\boldsymbol{\nabla}^2 V_\mathrm{m} = 0. \tag{5}$$

2.2. Pulsed eddy current field equations of the coil

As the displacement current is much less than the conduction current in the EMAT coils, the displacement current can be neglected. The magnetic vector potential satisfies the following equation[13]

$$\sigma \frac{\partial \boldsymbol{A}}{\partial t} - \frac{1}{\mu} \nabla^2 \boldsymbol{A} = \boldsymbol{J}_\mathrm{s}, \tag{6}$$

where $\boldsymbol{A}$ is magnetic vector potential, $\boldsymbol{J}_\mathrm{s}$ is source current density and σ is electrical conductivity.

The eddy current density in the coil conductors and in the skin depth of the specimen is

$$\boldsymbol{J}_\mathrm{e} = -\sigma \frac{\partial \boldsymbol{A}}{\partial t}. \tag{7}$$

In the area of the conductors, the distributions of the source current density and eddy current density are determined by the total current, the sectional area of the conductor and the distance between the conductors. In Eq. (6), there are two variables if the skin effect and proximity effect are considered. Therefore, another constraint equation must be provided for solving the two variables. In fact, the total current in the conductors is a known condition and can be described as

$$i(t) = \iint_{\Omega_\mathrm{c}} \boldsymbol{J} \mathrm{d}s = \iint_{\Omega_\mathrm{c}} (\boldsymbol{J}_\mathrm{s} + \boldsymbol{J}_\mathrm{e}) \mathrm{d}s, \tag{8}$$

where Ω_c represents the area of the coil section, $\boldsymbol{J}$ is the total current density. In other areas, the source current density $\boldsymbol{J}_\mathrm{s}$ in Eq. (6) is 0.

When $\boldsymbol{A}$ is solved, the Lorentz force in the specimen can be calculated through

$$\boldsymbol{f}_\mathrm{L} = \boldsymbol{J}_\mathrm{e} \times \boldsymbol{B}_0, \tag{9}$$

where $\boldsymbol{f}_\mathrm{L}$ is the Lorentz force.

2.3. The acoustic field equation of the specimen

It is assumed that the specimen is isotropic and satisfies linear elasticity and the continuity hypothesis. The elastic deformation of the specimen occurs

by the action of the body force $\boldsymbol{f}$. The equation of motion of the specimen is given by[14,15]

$$\boldsymbol{\nabla}\cdot\boldsymbol{T}+\boldsymbol{f}=\rho\frac{\partial^2\boldsymbol{u}}{\partial t^2}, \tag{10}$$

where $\boldsymbol{T}$ is the stress, $\boldsymbol{f}=\boldsymbol{f}_{\rm L}$ is the body force, $\boldsymbol{u}$ is the displacement, ρ is the density.

According to the relationship between $\boldsymbol{T}$ and $\boldsymbol{u}$,[12] equation (10) can be described by particle displacement

$$G\nabla^2\boldsymbol{u}+(G+\lambda)\nabla(\boldsymbol{\nabla}\cdot\boldsymbol{u})+\boldsymbol{f}_{\rm L}=\rho\frac{\partial^2\boldsymbol{u}}{\partial t^2}, \tag{11}$$

where λ and G are the Lame constants.

3. Consideration of voltage excitation

The method of dealing with the voltage excitation problem of EMATs is that the current excitation signal should be obtained in terms of the voltage excitation signal first, then, the multi-field coupled problem can be analysed by the equations in Section 2.

No matter how the coils of the EMATs are supplied by narrow pulses, by general tone burst signals or windowing tone burst signals, the excitation signal can always be approximately expressed by the superposition of a series of cosine functions

$$u(t)=\sum_{k=1}^{N}U_k\cos(\omega_k t+\phi_k),\quad 0\le t\le T, \tag{12}$$

where $k=1,2,\ldots,N$, U_k is the amplitude of the harmonic component of order k, ω_k is the angular frequency of the fundamental wave, φ_k is the phase angle, T represents the duration of the excitation signal.

In Eq. (12), U_k, ω_k, and φ_k can be obtained numerically by fast Fourier transformation (FFT). If the equivalent circuit parameters of the coil and specimen system are known, the current response under each frequency can be calculated according to Ohm's law. Thus, the current excitation signal can be obtained through inverse FFT (IFFT). Here, we call this method the FFT–IFFT method.

Since the frequency of the excitation signal is very high, eddy, skin and proximity effects should be considered. Therefore, the alternating current (AC) resistance and inductance of the coil will change with the excitation frequency, the geometric configuration and the electrical characteristics of the coils and specimen.

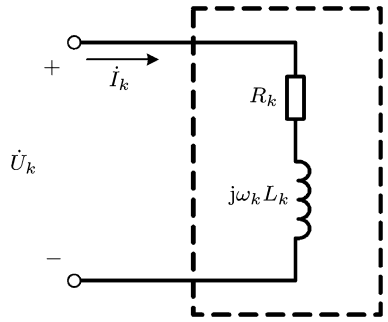


Fig. 1. Equivalent two-port network of coil.

For a specified frequency, resistance and inductance of the coil can be calculated through sinusoidal steady-state analysis of circuit-field coupling. For the system of the coil and specimen, the capacitance value is very small and can be neglected. Then, the system of the coil and specimen can be viewed as a two-port network, as shown in Fig. 1. The excitation voltage of EMATs is the port voltage and the excitation current is the port current. Thus, the complex power can be expressed as

$$\begin{aligned}\tilde{S}_k=\dot{\boldsymbol{U}}_k\dot{\boldsymbol{I}}_k^*&=(R_k+\mathrm{j}\,\omega_k L_k)\dot{\boldsymbol{I}}_k\dot{\boldsymbol{I}}_k^*\\&=R_kI_k^2+\mathrm{j}\,\omega_k L_kI_k^2,\end{aligned} \tag{13}$$

where $\tilde{S}_k$ represents the complex power, $\dot{\boldsymbol{U}}_k$ represents the port voltage, $\dot{\boldsymbol{I}}_k$ represents the port current, $\dot{\boldsymbol{I}}_k^*$ is the conjugate of $\dot{\boldsymbol{I}}_k$, I_k is the effective value of $\dot{\boldsymbol{I}}_k$. The R_k and L_k are the equivalent resistance and inductance of the two-port network, i.e. the AC resistance and inductance of the coil.

Neglecting the displacement current in the coil and specimen fields, we obtain the phase pattern of Poynting's theorem[16]

$$\begin{aligned}&-\iint_S(\dot{\boldsymbol{E}}_k\times\dot{\boldsymbol{H}}_k^*)\cdot\mathrm{d}\boldsymbol{s}\\&=\iiint_V\frac{1}{\sigma}J_k^2\mathrm{d}V+\mathrm{j}\iiint_V\omega\mu H_k^2\mathrm{d}V,\end{aligned} \tag{14}$$

where $\dot{\boldsymbol{E}}_k$ is the electrical field strength phasor quantity, $\dot{\boldsymbol{H}}_k^*$ is the conjugate of the magnetic field intensity phasor quantity $\dot{\boldsymbol{H}}_k$, J_k is the current density, H_k is the magnetic field intensity. In Eq. (14), the left part of the equation represents the electromagnetic complex power flowing into the field area close to the coil and specimen, the first term of the right part represents the dissipative active power, the second term of the right part represents dissipative reactive power.

Comparing Eq. (13) with Eq. (14), we obtain

$$R_k = \frac{1}{I_k^2} \iiint_V \frac{1}{\sigma} J_k^2 \mathrm{d}V, \tag{15}$$

$$L_k = \frac{1}{I_k^2} \iiint_V \mu H_k^2 \mathrm{d}V, \tag{16}$$

where ω is the angular frequency.

Therefore, when we calculate the impedance of the coil, we shall use the time harmonic field equation considering the eddy current effect, the skin effect and the proximity effect. By replacing the partial differential operator $\partial/\partial t$ with $\mathrm{j}\omega$ in Eqs. (6) and (8), we can express the time harmonic field equation as

$$\mathrm{j}\,\omega\sigma \boldsymbol{A} - \frac{1}{\mu}\nabla^2 \boldsymbol{A} = \boldsymbol{J}_\mathrm{s}, \tag{17}$$

$$\boldsymbol{I} = \iint_{\Omega_\mathrm{c}} (\boldsymbol{J}_\mathrm{s} + \boldsymbol{J}_\mathrm{e}) \mathrm{d}s. \tag{18}$$

Accordingly,

$$\boldsymbol{J}_\mathrm{e} = -\mathrm{j}\,\omega\sigma \boldsymbol{A}, \tag{19}$$

$$\boldsymbol{J} = \boldsymbol{J}_\mathrm{s} + \boldsymbol{J}_\mathrm{e}, \tag{20}$$

$$\boldsymbol{H} = \frac{1}{\mu}\boldsymbol{\nabla} \times \boldsymbol{A}. \tag{21}$$

When $\boldsymbol{J}$ and $\boldsymbol{H}$ are determined, the resistance R_k and inductance L_k of the coil can be calculated according to Eqs. (15) and (16).

4. Finite element modelling

According to the multi-field coupled equations given in Section 2, the Lorentz force is the critical quantity for transforming electromagnetic energy to mechanical energy. When the Lorentz force is determined, the particle displacement can be obtained in terms of the elastic theory. In this paper, the Lorentz force was viewed as the main research object. Therefore, the static magnetic field and pulsed eddy current field were calculated here.

Before calculating the equations by the FEM method, discretization should first be performed. The variables in Eqs. (5), (6), and (7) at each finite element node are expressed by the interpolating polynomial as

$$V_\mathrm{m} = \sum_i N_i V_{\mathrm{m}i}, \tag{22}$$

$$\boldsymbol{A} = \sum_i N_i \boldsymbol{A}_{\mathrm{m}i}, \tag{23}$$

$$\boldsymbol{J}_\mathrm{s} = \sum_i N_i \boldsymbol{J}_{\mathrm{s}i}, \tag{24}$$

where N_i is the interpolation function.

Equations (5), (6), and (8) are discretized by the Garlerkin method.[17] Through weighting residuals, substituting Eqs. (22)–(24) into all elements and merging the boundary conditions, we obtain the discretized matrix system of equations:

$$[K_\mathrm{V}][V_\mathrm{m}] = [Q_\mathrm{V}], \tag{25}$$

$$\frac{1}{\mu}[K_\mathrm{A}][\boldsymbol{A}] + \sigma[C_\mathrm{A}]\left[\frac{\partial \boldsymbol{A}}{\partial t}\right] - [D_\mathrm{A}][\boldsymbol{J}_\mathrm{s}] = [Q_\mathrm{A}], \tag{26}$$

$$[M][\boldsymbol{J}_\mathrm{s}] - \sigma[N]\left[\frac{\partial \boldsymbol{A}}{\partial t}\right] = [i], \tag{27}$$

where $[K_\mathrm{V}]$, $[K_\mathrm{A}]$ are the stiff matrixes; $[C_\mathrm{A}]$, $[D_\mathrm{A}]$, $[M]$, $[N]$ are the coefficient matrixes; $[Q_\mathrm{V}]$, $[Q_\mathrm{A}]$ are the boundary integration vector. $[V_\mathrm{m}]$, $[\boldsymbol{A}]$, $[\boldsymbol{J}_\mathrm{s}]$, $[i]$ are scalar magnetic potential vector, magnetic vector potential vector, source current density vector and current vector, respectively. The full expressions of the matrixes are given in Ref. [17].

Substituting Eq. (27) into Eq. (26), we can obtain

$$\frac{1}{\mu}[K_\mathrm{A}][\boldsymbol{A}] + \sigma([C_\mathrm{A}] - [D_\mathrm{A}][M]^{-1}[N])\left[\frac{\partial \boldsymbol{A}}{\partial t}\right] - [D_\mathrm{A}][M]^{-1}[i] = [Q_\mathrm{A}]. \tag{28}$$

As the calculations of the pulsed current magnetic field and displacement are transient processes, the time-step method is used. The differential terms in Eq. (28) is given by backward difference equations as

$$\left[\frac{\partial \boldsymbol{A}}{\partial t}\right] = \frac{1}{\Delta t}([\boldsymbol{A}]_{t+\Delta t} - [\boldsymbol{A}]_t), \tag{29}$$

where t is the time, Δt is the time step.

Substituting Eq. (29) into Eq. (28), we obtain the time-step FEM equations as

$$\left(\frac{1}{\mu}[K_\mathrm{A}] + \frac{\sigma}{\Delta t}([C_\mathrm{A}] - [D_\mathrm{A}][M]^{-1}[N])\right)[\boldsymbol{A}]_{t+\Delta t} - \frac{\sigma}{\Delta t}([C_\mathrm{A}] - [D_\mathrm{A}][M]^{-1}[N])[\boldsymbol{A}]_t - [D_\mathrm{A}][M]^{-1}[i]_{t+\Delta t} = [Q_\mathrm{A}]_{t+\Delta t}. \tag{30}$$

The FEM equations of time harmonic field equations (17) and (18) can be obtained by replacing $[\partial \boldsymbol{A}/\partial t]$ with $\mathrm{j}\,\omega[\boldsymbol{A}]$ in Eq. (30). Thus, we obtain

$$\left(\frac{1}{\mu}[K_\mathrm{A}] + \mathrm{j}\,\omega\sigma([C_\mathrm{A}] - [D_\mathrm{A}][M]^{-1}[N])\right)[\boldsymbol{A}] - [D_\mathrm{A}][M]^{-1}[I] = [Q_\mathrm{A}]. \tag{31}$$

5. Calculation and experiments for an EMAT model

5.1. Calculation and experimental model

A kind of EMAT for generating a Lamb[18] wave is shown in Fig. 2. The EMAT is comprised of a square permanent magnet with a perpendicular magnetic field, a meander coil and a specimen. The permanent magnet is made of NdFeB material. The meander coil is made by PCB technique, i.e., the coil consists of rectangular copper traces on a fibre glass substrate. The copper traces lie on both faces of the substrate. Therefore, it is a two-layer structure coil. In each layer, there are eight meander belts. Each belt has two rectangular copper traces. We call the kind of coil a two-layer two-bundle coil. The rectangular copper traces in the same meander belt have the same current direction. The current directions between two adjacent belts are opposite. The distance between two adjacent belts equals half the wavelength of the generated Lamb wave.

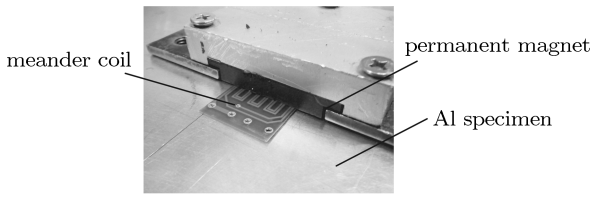


Fig. 2. A kind of EMAT for generating Lamb wave comprised of NdFeB permanent magnet, PCB meander coil and Al specimen.

In the Cartesian coordinate system, the dimensions of the permanent magnet, coil and specimen in the z axis direction is assumed to be infinitely long. If the ends effect of the coil is neglected, the model of EMAT in Fig. 2 can be viewed as a two-dimensional (2D) model in x–y plane.

The 2D model of the EMAT is shown in Fig. 3(a). The static magnetic field of the permanent magnet has the components $\boldsymbol{B}_{0x}$ and $\boldsymbol{B}_{0y}$, while magnetic vector potential of the pulse magnetic field only has the component $\boldsymbol{A}_z$.

In Fig. 3(a), the residual flux density of the permanent magnet is 1 T. The dimensions of the permanent magnet are $w_{\rm p1} = 40$ mm; $w_{\rm p2} = 5$ mm; $h_{\rm p} = 8$ mm. The aluminum specimen's parameters are: conductivity $\sigma_{\rm Al} = 3.5 \times 10^7$ S/m; $w_{\rm A} = 60$ mm; $h_{\rm A} = 5$ mm. The meander coil is made by copper with conductivity $\sigma_{\rm Cu} = 2.667 \times 10^7$ S/m. The dimensions of the coil are $a = 0.035$ mm, $b = 0.72$ mm. The layer distance is $h_{\rm c} = 0.5$ mm. The wave length is $\lambda_{\rm L} = 6.4$ mm.

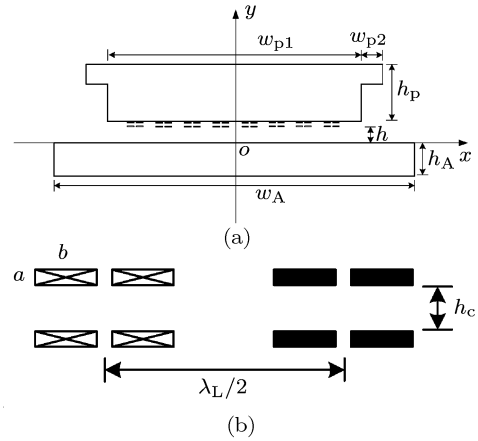


Fig. 3. The 2D model of the EMAT in x–y plane: (a) global model; (b) two-layer two-bundle meander coil configuration.

In the experiments, a radio frequency (RF) power amplifier (AG1024), which could provide continuous sine signal and tone burst signal, was supplied to the meander coil. An oscilloscope which can record the wave data was used to measure the voltages of the coil and a 1 Ω sample resistance which was connected in series with the coil. Thus, the current of the coil can be obtained according to the voltage of the sample resistance. The resistance and inductance of the coil can be calculated in terms of the measured continuous sine voltage and current signal. The tone burst voltage and current signals used for generating the acoustic waves can also be measured. One pair is shown in Fig. 4 when the lift-off was $h = 0.1$ mm.

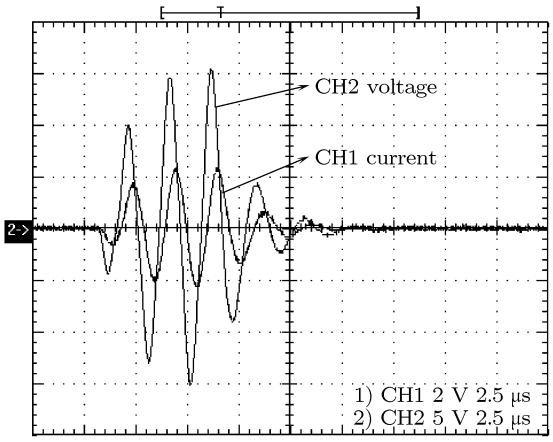


Fig. 4. Measured pulsed voltage and current signals of the coil. The frequencies of the tone burst signals are 500 kHz. The period number is 3.

In the calculation process, the measured voltage signal in Fig. 4 was used as the pulsed voltage excitation. As mentioned in Section 3, the pulsed current

must be calculated first by the FFT–IFFT method. Then, the Lorentz force was calculated using the coupled FEM model. The calculation steps are shown in Fig. 5.

5.2. Results comparison and analysis

The resistances and inductances of the coil were calculated at frequencies of 500, 750, and 250 kHz in order to verify the validity of the proposed method. Through solving the time harmonic field equation, the resistances and inductances at the lift-off distance 0.5, 1, and 2 mm were calculated according to Eqs. (15) and (16). The calculated and measured results are shown in Table 1.

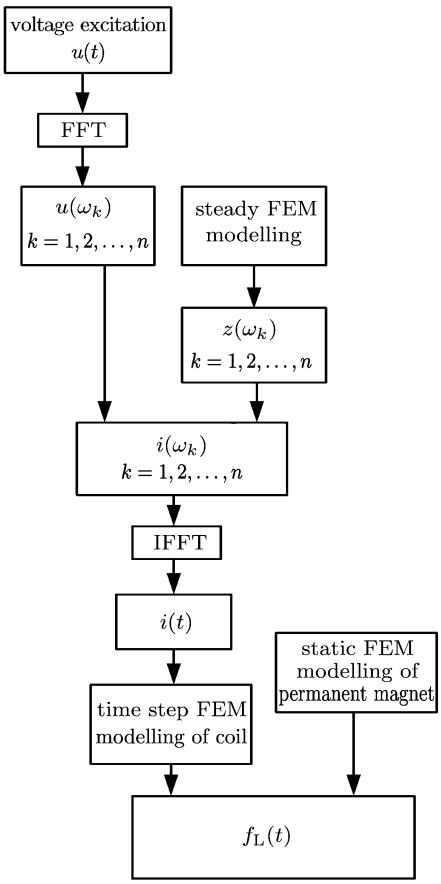


Fig. 5. The calculated flow chart of Lorentz force.

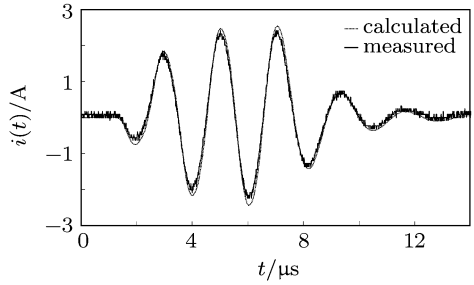


Fig. 6. Calculated and measured current signals.

In Table 1, the subscripts c and m indicate the calculated and measured results, respectively. Comparing the calculated results with the measured ones, we can find that they are in good agreement, which verifies the correctness of the proposed method. The reason that the measured results are a little larger than the calculated ones is that the ends of the coil are neglected. In Table 1, the resistance of the coil decreases with the lift-off distance while increasing with excitation frequency. The inductance of the coil increases with both lift-off distance and excitation frequency.

The calculated and measured current signals at the lift-off distance 1 mm are shown in Fig. 6. We can find that both the amplitudes and phase positions are in good agreement, which verifies the validity of the proposed FFT–IFFT method and impedance calculation formulas.

Figures 7 and 8 give Lorentz force density as a function of time under the third source conductor from the left near the surface of an aluminum specimen, when the static magnetic flux is provided by a permanent magnet with residual magnetic flux density 1 T and the voltage excitation is kept the same. It is found that since the biased magnetic field of the permanent magnet is not only in one direction, both components of Lorentz force density in horizontal and vertical directions exist. The amplitude of $f_{\mathrm{L}x}$ is larger than that of $f_{\mathrm{L}y}$ in the presented permanent magnet. The amplitudes of $f_{\mathrm{L}x}$ and $f_{\mathrm{L}y}$ both decrease with the lift-off distance of the coil.

Table 1. Coil impedances under different frequencies and lift-off distances.

Lift-off	500 kHz				750 kHz				250 kHz			
	$R_{1\mathrm{c}}/\Omega$	$R_{1\mathrm{m}}/\Omega$	$L_{1\mathrm{c}}/\mu\mathrm{H}$	$L_{1\mathrm{m}}/\mu\mathrm{H}$	$R_{2\mathrm{c}}/\Omega$	$R_{2\mathrm{m}}/\Omega$	$L_{2\mathrm{c}}/\mu\mathrm{H}$	$L_{2\mathrm{m}}/\mu\mathrm{H}$	$R_{3\mathrm{c}}/\Omega$	$R_{3\mathrm{m}}/\Omega$	$L_{3\mathrm{c}}/\mu\mathrm{H}$	$L_{3\mathrm{m}}/\mu\mathrm{H}$
0.5 mm	2.50	2.62	1.22	1.28	2.59	2.65	1.20	1.28	2.40	2.52	1.24	1.34
1 mm	2.44	2.51	1.49	1.52	2.54	2.60	1.48	1.52	2.35	2.40	1.51	1.55
2 mm	2.40	2.46	1.67	1.73	2.50	2.55	1.66	1.71	2.32	2.35	1.68	1.72

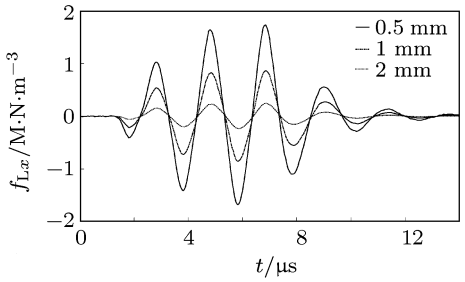


Fig. 7. Horizontal component of Lorentz force density f_{Lx} as a function of time t at lift-off distances 0.5 mm, 1 mm and 2 mm.

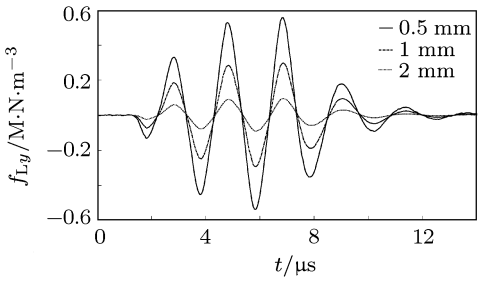


Fig. 8. Vertical component of Lorentz force density f_{Lx} as a function of time t at lift-off distances 0.5 mm, 1 mm and 2 mm.

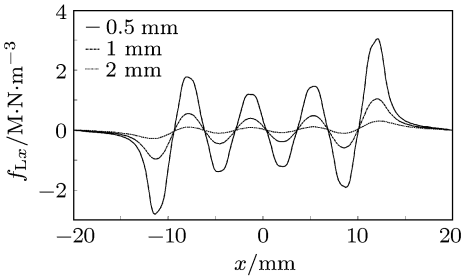


Fig. 9. Horizontal component of the Lorentz force density distribution along the surface of the specimen at the time 6.85 μs at lift-off distances 0.5 mm, 1 mm and 2 mm.

Figures 9 and 10 show the distribution of f_{Lx} and f_{Ly} along the surface of the specimen, as a function of position. They illustrate that the specimen is driven by the Lorentz force in opposite directions under adjacent coil belts. The amplitudes of the Lorentz force density under different coil belts vary greatly due the non-uniform distribution of the permanent magnet, especially for f_{Ly}.

To compare the differences between the models and analysis methods in former literatures and in this paper, the calculated current excitation as a constant quantity was used to calculate the Lorentz force density in the specimen, keeping the static magnetic flux as 1 T uniform.

Figure 11 shows the Lorentz force density under the third source conductor from the left near the surface of an aluminum specimen under lift-off distances 0.5 mm, 1 mm and 2 mm when the static magnetic flux is assumed to be a constant value 1 T and the current excitation is kept the same. Since the static magnetic field is perpendicular or parallel to the specimen surface, the Lorentz force has only an x or a y component.

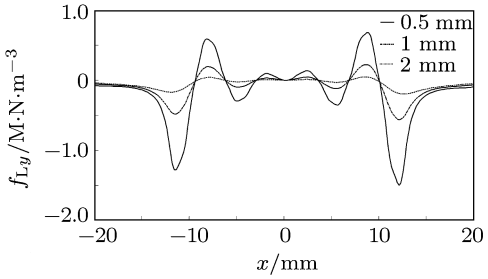


Fig. 10. Vertical component of the Lorentz force density distribution along the surface of the specimen at the time 6.85 μs at lift-off distances 0.5 mm, 1 mm, and 2 mm.

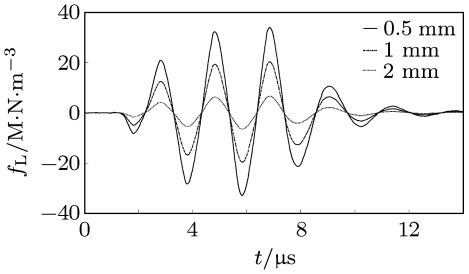


Fig. 11. Lorentz force density in the specimen under uniform static magnetic flux 1 T.

Figure 12 shows the Lorentz force density distribution along the surface of the specimen under lift-off distances 0.5 mm, 1 mm, and 2 mm when the static magnetic flux has a constant value 1 T and the current excitation is kept the same. Owing to the uniform distribution of the biased magnetic field, the distribution of Lorentz force density is more uniform under different coil belts. Therefore, neglecting the non-uniformity of the static magnetic field will cause a large calculation error when we simulate the performance of the EMATs.

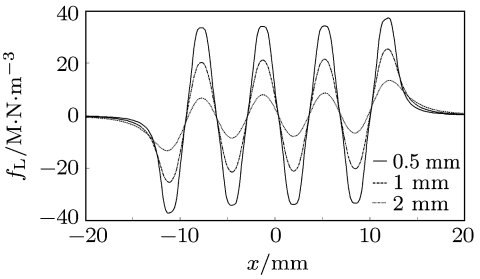


Fig. 12. Lorentz force density distribution in the specimen surface under uniform static magnetic flux 1 T at the time 6.85 μs.

6. Conclusion

Generally, voltage excitation is supplied to the coil of EMATs and the biased magnetic field is non-uniform for the actual EMATs. A complete model of EMATs, including a non-uniform biased magnetic field, a pulsed eddy current field and a acoustic field, was set up. The exciting current was obtained according to the exciting voltage and impedances calculated by the circuit-field coupled method. The FEM model was presented and used to analyse the Lorentz force in the specimen that drives the generation of ultrasonic waves under voltage excitation. The analysis of a practical Lamb wave EMAT shows the correctness and validity of the presented model and method. The proposed method, which realized the simulation and analysis of the EMATs under voltage excitation, is beneficial for improving the design of EMATs. The lift-off effect and the influence of neglecting the non-uniform distributions were studied. The influence of lift-off distance under the same voltage was more obvious than that under the same current. Neglecting the non-uniformity of the static magnetic field will result in EMAT calculation errors.

References

[1] Masahiko H and Hirotsugu O 2003 *EMATs for Science and Industry Non-contacting Ultrasonic Measurements* (Boston: Kluwer Academic publishers)

[2] Zhou D, Liu X Z, Gong X F, Nazarov V E and Ma L 2009 *Chin. Phys.* B **18** 898

[3] Mirkhani K, Chaggares C, Masterson C, Jastrzebshi M, Dustko T, Sinclair A, Shapoorabadi R J, Konrad A and Papini M 2004 *NDT & E. Int.* **37** 181

[4] Jian X, Dixon S, Grattan K T and Edwards R S 2006 *Sens. Actuators* A **128** 296

[5] Thompson R B 1977 *J. Appl. Phys.* **12** 4942

[6] Thompson R B 1979 *Appl. Phys. Lett.* **34** 175

[7] Ludwig R, You Z and Palanisamy R 1993 *IEEE Trans. Magn.* **29** 2081

[8] Jafri-Shapoorabadi R, Konrad A and Sinclair A N 2002 *IEEE Trans. Magn.* **38** 617

[9] Jafri-Shapoorabadi R, Konrad A and Sinclair A N 2005 *J. Appl. Phys.* **97** 10

[10] Eskandarzade M, Kundu T, Liebeaux N, Placko D and Mobadersani F 2010 *Ultras.* **50** 583

[11] Hussein A M 1991 *IEEE Trans. Magn.* **27** 4258

[12] William J H 1972 *IEEE Trans. Magn.* **8** 3

[13] Weiss J and Csendes Z J 1982 *IEEE Trans. Power Apparatus Syst.* **PAS101** 3796

[14] EISLEY J G 1989 *Mechanics of Elastic Structures: Classical and Finite Element Methods* (Englewood Cliffs: Prentice Hall)

[15] Huang B, Zhang Y L, Zhang D and Guo X F 2010 *Chin. Phys.* B **19** 054302

[16] Guru S 2004 *Electromagnetic Field Theory Fundamentals* (Boston: PWS Pub.)

[17] Jin J M 2000 *The Finite Element Method in Electromagnetics* (New York: Wiley)

[18] Li S, Okada T, Chen X M and Dai H W 2007 *IEEJ Trans. Elec. Inf. Syst.* **127** 367